Coseismic damage and softening of fault rocks at seismogenic depths

W. Ashley Griffith [a,*], Thomas M. Mitchell [b,c], Jörg Renner [b], Giulio Di Toro [c,d]

[a] Department of Geology and Environmental Science, University of Akron, Akron, Ohio, United States
[b] Institut für Geologie, Mineralogie und Geophysik, Ruhr-Universität Bochum, Bochum, Germany
[c] Istituto Nazionale di Geofisica e Vulcanologia, Roma, Italy
[d] Dipartimento di Geoscienze, Università di Padova, Padova, Italy

ARTICLE INFO

ABSTRACT

Elastic stiffness, a critical property for stress-orientation, propagation of earthquake ruptures and associated seismic waves, and the capability of crustal rocks to store strain energy, is expected to be highly variable throughout the seismic cycle due to complex sequences of damage and healing. Post-seismic healing and exhumation-related alteration render it impossible to assess how well rock stiffness as measured in the laboratory on samples collected from fault zones represents *in situ*, coseismic rock stiffness at seismogenic depths. Here we estimate the *in situ*, coseismic stiffness of fault rocks from the pseudotachylyte-bearing Gole Larghe Fault Zone (Italian Southern Alps), using aspect ratio measurements of pseudotachylyte injection veins and numerical simulations. Aspect ratios of injection veins cutting across tonalite and cataclasite exhibit a maximum vein aperture positively correlating with vein length. To model vein opening, fault and injection veins are assumed to be filled with pressurized melt. Consistent with recent results from studies of melt lubrication we assume that the magnitude of the melt pressure is in equilibrium with the *fault-normal* stress and the fault vein approximately maintains constant thickness during slip. The numerical simulations of injection vein opening due to pressurized frictional melt indicate that the average *in situ* coseismic stiffness of the wall rocks is 5–50 times smaller than the stiffness obtained from laboratory measurements on the same rocks in their present-day state. The disagreement between laboratory measurements and simulations brings into question the appropriateness of using laboratory-derived values for rock stiffness to model coseismic processes at depth.

1. Introduction

The bulk elastic stiffness of faulted crust constrains the amount of elastic strain energy that can be stored during tectonic loading and released during earthquakes and also exerts a direct control on the earthquake rupture velocity (Biegel et al., 2008). Near-fault stiffness changes can result in significant stress rotation, allowing faults to slip under less-than-optimal far-field stress states (Rice 1992; Faulkner et al., 2006). Therefore evolution of rock stiffness during earthquakes is critical to understanding seismic rupture nucleation, propagation, and arrest. Fracture and pulverization damage surrounding crustal scale faults can result in stiffness reductions of ~40% over large fault-normal distances (> 1 km) and up to 8 km depth, and this softening has been shown to persist 1 ky or more (Cochran et al., 2009; Li et al., 1994, 1998, 2006). At critical seismogenic depths, pressure, temperature, and fluid flow tend to increase the degree and rate of healing of damaged rocks (e.g. Brantley et al., 1990; Moore et al., 1994; Morrow et al., 2001; Tenthorey and Cox, 2006; Tenthorey and Fitz Gerald, 2006). Several studies document significant coseismic drops in velocity, believed to be associated with rupture-induced damage, followed by time dependent increases in velocity over timescales of 2–10 yr (Brenguier et al., 2008; Hiramatsu et al., 2005; Vidale and Li, 2003). Direct and indirect observations constrain *in situ* rock mechanical properties along seismogenic faults to ~3 km (i.e., San Andreas Fault Observatory at Depth drilling project, Zoback et al., 2010) and ~8 km depth (e.g., Cochran et al., 2009; Li et al., 2006).

The fact that fault rock stiffness evolves throughout the seismic cycle presents a conundrum for scaling laboratory-derived rock properties which can vary with damage-related elastic stiffness changes (e.g., hydraulic conductivity, compressibility, and thermal expansion coefficient) to natural fault processes. For example, theoretical models of coseismic processes, such as sliding friction and heat and pore-fluid flow, are based on laboratory measurements of rock properties (e.g. Lachenbruch, 1980; Noda and Shimamoto, 2005; Rice, 2006). These measurements in the laboratory are performed on specimens collected

---

* Corresponding author. Tel.: +1 330 972 7632; fax: +1 330 972 7611.
E-mail address: wag8@uakron.edu (W.A. Griffith).

from exhumed fault zones, or from boreholes much shallower than typical seismogenic depths (e.g., Faulkner et al., 2006). Given that significant healing has taken place during exhumation (e.g., Gratier et al., 2003; Faulkner et al., 2006), use of such laboratory results in modeling relies on potentially biased estimates of rock properties.

Our study addresses the questions: (1) "What is the *maximum* reduction in rock stiffness near a fault at seismogenic depths?" and (2) "How does this estimate compare to laboratory measurements on rocks collected from exhumed fault zones?". Answering (1) requires one to eliminate effects of the poorly-constrained healing process at depth. Given that the damage source is fault rupture and slip, one thus has to find the *in situ*, *coseismic* rock stiffness. We estimate this *in situ*, *coseismic* rock stiffness by simulating the formation of injection veins, interpreted to represent coseismic fault structures found along pseudotachylyte (solidified melt derived from frictional heating) bearing faults. Presumably, simulations matching our field observations best constrain stiffness at the time of vein formation. Question (2) can be answered by comparing our modeled values to laboratory data for samples from the analyzed outcrops.

2. Geologic background: The Gole Larghe Fault Zone

During the last decade, abundant evidence has been reported for seismic slip along the Gole Larghe Fault Zone (GLFZ), Southern Alps, Italy (Di Toro and Pennacchioni, 2004, 2005). The GLFZ is a right-lateral strike slip fault-zone with a minor reverse slip component that cuts east-to-west across the Adamello tonalitic batholith, and comprises hundreds of individual fault strands across a zone ∼500 m wide (Di Toro and Pennacchioni, 2005). Fault strands hosting pseudotachylytes, generally accepted as evidence of seismic slip (Sibson, 1975), nucleated on pre-existing joints at depths of 9–11 km at ambient temperatures of 250–300 °C approximately 30 Ma ago (Di Toro and Pennacchioni, 2004; Pennacchioni et al., 2006). In the GLFZ, fault strands cut and offset abundant aplite dikes, and fault rocks on individual strands consist either of cataclasite, cataclasite overprinted by pseudotachylyte, or, in rare cases, only pseudotachylytes. Pseudotachylyte veins are easily distinguished from the host tonalite and cataclasite in polished outcrops at the base of the Lobbia glacier (Fig. 1a and b), and occur as abundant millimeter to centimeter thick fault and injection veins, or less commonly as pseudotachylyte breccias. Pseudotachylyte injection veins intrude both cataclasite and tonalite and range in length from sub-millimeter to approximately one meter.

3. Injection veins

3.1. Field observations

In general, pseudotachylyte injection veins within the GLFZ intrude the host tonalite, emanating from pseudotachylyte veins running along the fault surface (fault veins). Di Toro et al. (2005b) measured orientations of a large number of injection veins, and found that (1) > 70% occurred on the south side of the fault veins, and (2) two sets dominate: one making a small (15–25°) angle with the main fault veins (Set I), and one almost orthogonal to the fault veins (Set II). Set II injection veins were likely formed as virgin fractures near propagating earthquake rupture tips whereas Set I injection veins are parallel to and intrude pre-existing minor cataclasite faults persisting throughout the GLFZ (Di Toro et al., 2005b). Some isolated pseudotachylyte injection
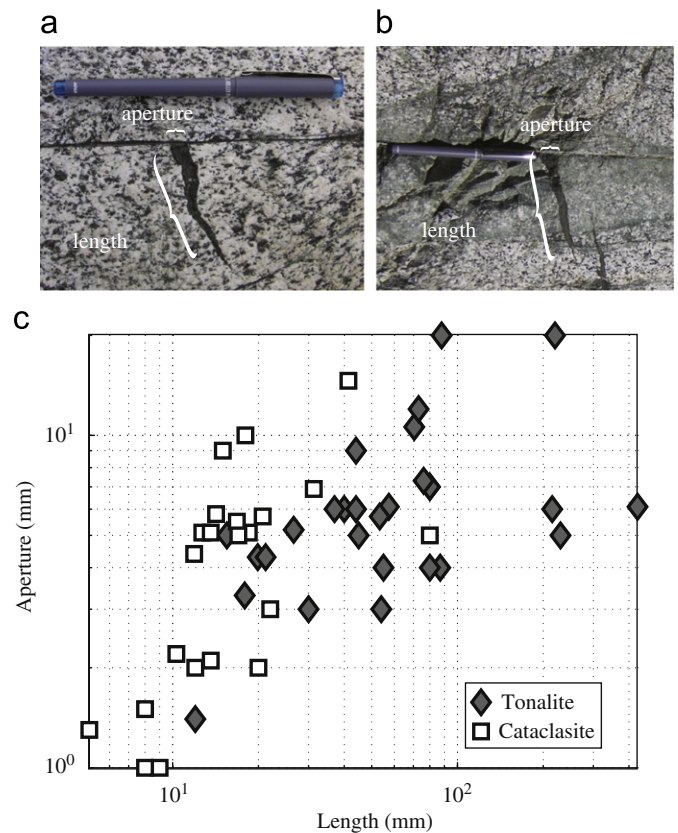

Fig. 1. Injection vein field photos and data. (a) Injection vein cutting tonalite, (b) injection vein cutting cataclasite, and (c) aperture and length of pseudotachylyte injection veins which cut cataclasite (empty squares) and tonalite (gray diamonds) in the Gole Larghe Fault Zone.

veins and reservoirs are also located at bends and stepovers along faults (e.g., Di Toro et al., 2005a).

Displacement across the injection veins is principally opening, and the maximum aperture is typically at their base (i.e., the point of intersection with the fault vein, Fig. 1). In general, injection vein opening distribution is that of a half-bell, tapering rapidly from the vein base and less rapidly toward the tip. Injection veins extending variable distances into the wall rock are most commonly truncated by other fractures, and less-frequently terminate at discrete tips in otherwise monolithic rock.

Measurement of > 50 injection veins reveal a positive correlation between maximum aperture and length (Fig. 1c). The outcrop surface in most cases is glacially-polished allowing us to view the injection veins in great detail. However, the hummocky nature of the outcrop surface means that exposures are not exactly perpendicular to the injection veins potentially biasing aperture measurements. We took care to correct for this distortion geometrically, so aperture measurements should reflect the true aperture closely. The errors are acceptable since most injection veins do not deviate far from being perpendicular to the exposure surface and the apparent aperture (A_{ap}) as exposed in the field differs from the true aperture (A) by only 10% for exposures that deviate from vein-perpendicular by as much as $\alpha = 25°$ because $A_{ap} = A/\cos \alpha$.

3.2. Microstructural observations

Based on field observations revealing that the displacement across veins is primarily opening, pseudotachylyte injection veins have been interpreted as fluid-filled mode I cracks (e.g., Sibson, 1975; Grocott, 1981; Swanson, 1992; Di Toro et al., 2005a,b).
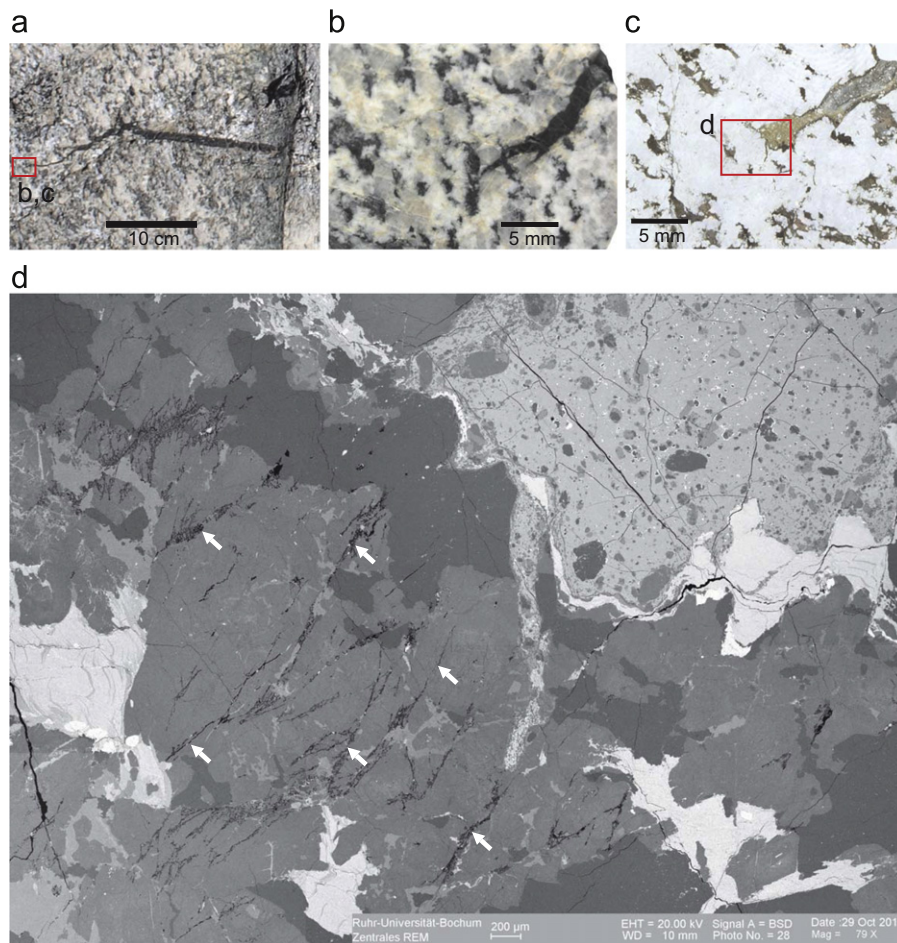
Fig. 2. Microstructure associated with injection vein tip terminating in virgin tonalite. (a) The injection vein grew straight, sub-perpendicular from the fault vein and kinked near its end, (b) a core drilled at the tip shows, (c) a blunt tip in thin section and (d) SEM-BSE image shows an array of cracks (indicated by white arrows) forming the process zone at the pseudotachylyte injection vein tip.

This interpretation provides a critical constraint on the local stress state during opening, as mode I fractures propagate along a plane whose unit normal vector parallels the minimum principal compressive stress, σ_3. To evaluate this assumption of failure mode, we examined the tip zone of an injection vein using optical and scanning electron (SEM) microscopy on a thin section cut perpendicular to the vein-tip line (Fig. 2). The vein tip is blunt, and completely filled with pseudotachylyte. In Back Scatter SEM images, several micrometers-thick cracks emanate from the vein tip, and are sub-parallel to the overall injection-vein trend as expected for small cracks composing the process zone of a fracture propagating in opening mode through a homogeneous and isotropic medium (e.g., Delaney et al., 1986). These observations are consistent with considering the investigated injection vein as having propagated as an opening mode crack, through virgin rock leaving a frozen process zone.

3.3. A conceptual model for injection vein formation

Opening displacement along injection veins is driven by injection of pressurized melt similar to igneous dike formation; the veins represent conduits along which melt can be extruded from the fault surface (Sibson, 1975). In many cases it is unclear whether the fractures hosting injected pseudotachylytes propagated ahead of the penetrating melt, or whether the fractures were inherited, or some combination of the two (Grocott, 1981). Swanson (1992) interpreted pseudotachylyte injection veins as a hydraulic fracture forming due to melt pressurization along the main fault vein. Such pressurization can be due to thermal expansion during solid–liquid phase transition; melting results in a volume increase of ~10–15% with respect to the pristine tonalite (Maddock et al., 1987). The observed unique asymmetry (pseudotachylyte injection veins in the GLFZ predominantly form on one side of the fault plane) suggests that vein formation is controlled by rupture directivity (Di Toro et al., 2005b). Asymmetry can be explained by the Mode II slip pulse model of Rice et al. (2005) predicting tensile crack generation near the shear rupture (earthquake) tip propagating close to Rayleigh wave speed, a mechanism experimentally verified by Griffith et al. (2009) and Ngo et al. (2012).

We idealize the general process of injection vein formation in a systematic way prone for modeling (Fig. 3): (1) the veins nucleate along a pre-existing fault surface; (2) injection of melt follows some pre-existing weak discontinuity (fractures in the wall rocks produced before (Set I) and during (Set II) the passage of the seismic rupture front); (3) the injection occurs in a region of transiently enhanced tensile least compressive stress due to the recent passage of a seismic rupture as evidenced by the vein asymmetric distribution; and (4) vein opening and further extension is driven by pressurized melt formed on the sliding fault surface behind the propagating rupture tip and extruded into the actively forming injection veins. Based on the thickness of the injection veins measured in the GLFZ ($\ll 1$ m), complications resulting from advective heat transfer and viscous heat
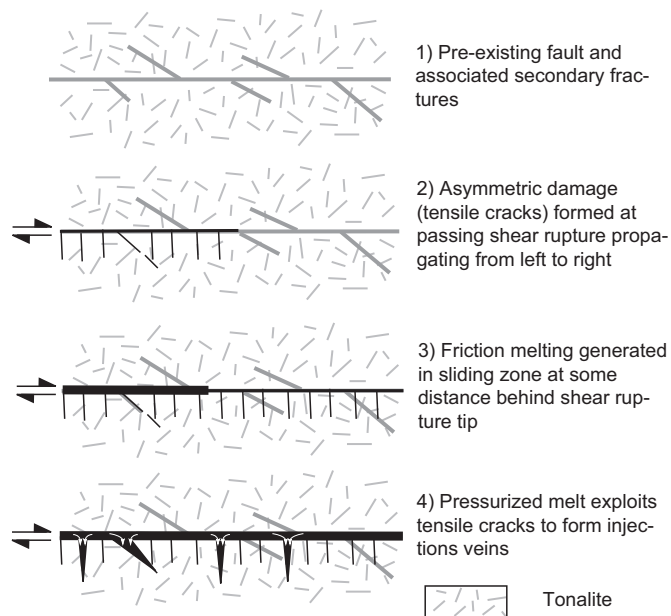
Fig. 3. Conceptual model of injection vein formation. In step (1), the fault is a structural discontinuity in an otherwise undamaged rock. In step 2, a rupture propagates towards the right across the fault, leaving a series of cracks or microcracks in its wake. In (3) and presumably later during the same sliding event (final step 4), pressurized, mobile melt is produced along the slipping zone at some distance from the rupture tip. In step (4), melt is injected along some of these cracks. Note that step (4) also applies to any other pre-existing off-fault discontinuities that might be exploited by melt during the slip event.

generation is likely not significant (Rubin, 1995); however solidification time due to conductive heat loss is expected to be much shorter at the tips, and longer at the vein base because of the tapered shape of veins.

4. Injection vein modeling

We use the final stage of injection vein development (Fig. 3) as an idealization for modeling the opening of a single injection vein (Fig. 4a). It is appealing to adopt analytical models for dike development (e.g., Pollard and Holzhausen, 1979; Delaney and Pollard, 1981; Delaney et al., 1986; Rubin, 1995) to injection vein mechanics as recently done by Rowe et al. (in press) who used the symmetric pressurized crack model of Rubin (1995) in a study on pseudotachylyte and clastic injection veins. Upon closer inspection, however, a finite length symmetric fluid filled crack embedded in an infinite medium as envisioned for dikes (e.g. Delaney and Pollard, 1981; Rubin, 1995) is incompatible with injection vein geometry, since the only plane of symmetry for the injection vein is its long axis (Fig. 4b). Instead, injection vein opening more closely resembles an edge crack in a semi-infinite half-plate due to the "free-edge effect" of the melt-filled fault vein (Fig. 4c). For the symmetric crack embedded in an infinite medium, the maximum opening is at its center, at which point the tangent of the crack wall must be parallel to the crack length (e.g., Sanford, 2003, pp. 82). For an edge crack in a half plate, the opening maximum is at the plate edges and the opening there is not restricted in the same way as for the symmetric crack (Fig. 4c). Due to this difference, both the maximum aperture and the stress intensity factor for an edge crack of length a will be larger than for a symmetric, finite length crack of length $2a$ embedded in an infinite medium when subjected to the same driving stress. Thus, the edge crack is allowed to open more with
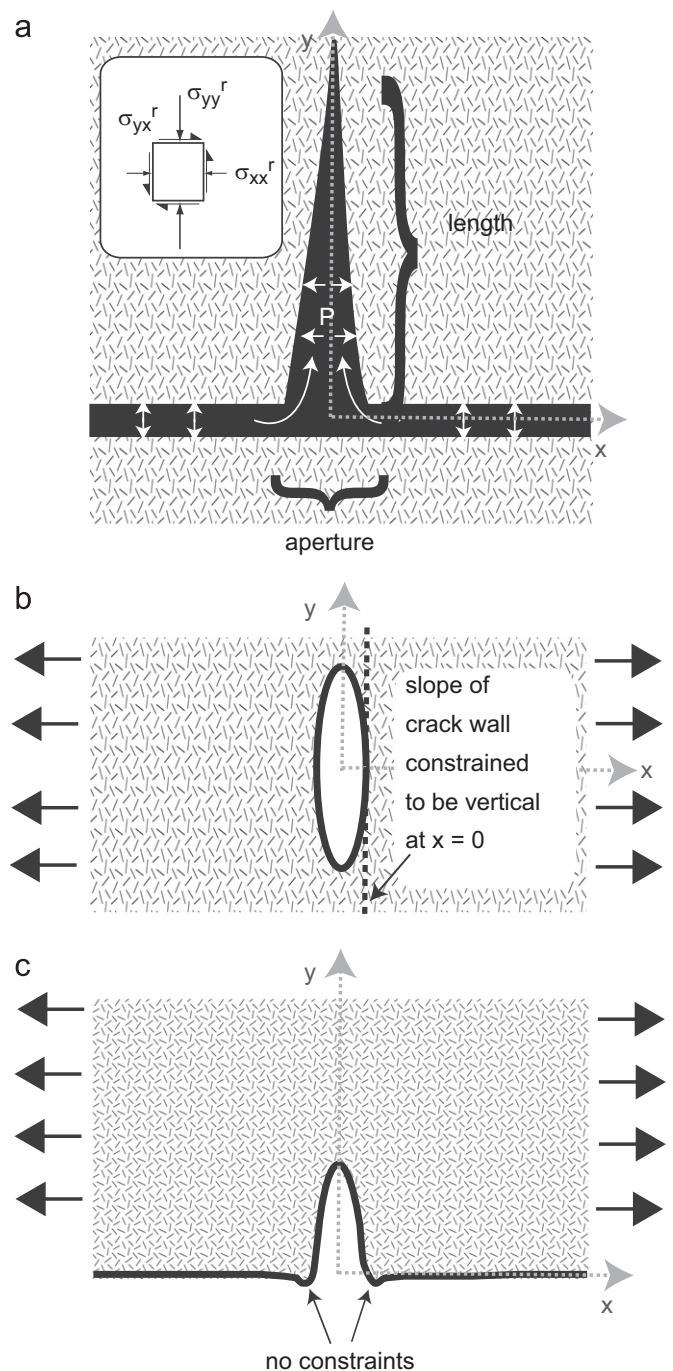

Fig. 4. Possible crack geometries and effects of model assumptions. (a) Model idealization, (b) embedded crack subjected to uniaxial extension, and (c) edge crack subjected to uniaxial extension. The model idealization more closely resembles an edge crack, because the slope of crack walls are not constrained where the injection vein intersects the faults, however frictional contact may occur along the fault.

the same driving stress and resisting rock stiffness than the fully embedded pressurized crack.

We model the process of injection vein opening as a quasi-static process in which a crack of fixed length is opened due to melt pressure. Because melt cooling times far exceed crack propagation times for pseudotachylyte injection veins (Rowe et al., in press), the preserved aperture of the injection vein is the *minimum* possible aperture, as injection veins could have closed slightly after initial opening, while the injection vein was still quenching. Given that

opening is driven by melt overpressure (the difference between the melt pressure and vein-perpendicular normal stress) and limited by the rock stiffness, the preserved aperture therefore provides an upper limit on possible rock stiffness.

4.1. Displacement discontinuity method

We model injection vein opening using the Displacement Discontinuity Method (DDM) (Crouch and Starfield, 1983, Chapter 5) in which surfaces can be represented as discretized boundaries (see Fig. 5 "Model View") with constant displacement discontinuities (i.e., relative displacement normal and parallel to each element is constant across the entire element). The DDM can solve for stress, strain, and displacement fields throughout an isotropic, homogeneous body as long as the boundary conditions (tractions or displacements) are prescribed along the model surfaces.

The injection vein model utilized in this study differs from a pressurized edge crack by the possibility for frictional slip on the edge, the fault vein, in case it should close locally. The contact problems are solved using a "complementarity" algorithm of O. Mutlu (Mutlu and Pollard, 2008) discussed in detail by De

Bremaecker and Ferris (2004). The algorithm uses six inequality constraints which prevent interpenetration, enforce a Coulomb sliding criterion, and allow for constant opening displacement discontinuity across each element. Because friction is a path-dependent process, solutions to the boundary value problem for a non-vanishing friction coefficient ($\mu \neq 0$) are non-unique and dependent on the prescribed loading path.

4.2. Model parameters and procedure

In all models, we prescribe a uniform remote stress as well as a fluid pressure along all elements comprising the fault and injection veins, and the DDM simultaneously solves for tractions and normal and shear displacement discontinuities (d_n and d_s respectively, Fig. 5a) along the elements. Herein "remote" and "far-field" stress refer not necessarily to the macroscopic tectonic stress state, but to a stress state that acts across a region much larger than the injection vein being modeled, practically speaking a region of radius no more than a few meters. The model assumes a straight injection vein oriented exactly perpendicular to a fault which is 10 times the length of the injection vein ($a_{fault} \gg a_{vein}$),
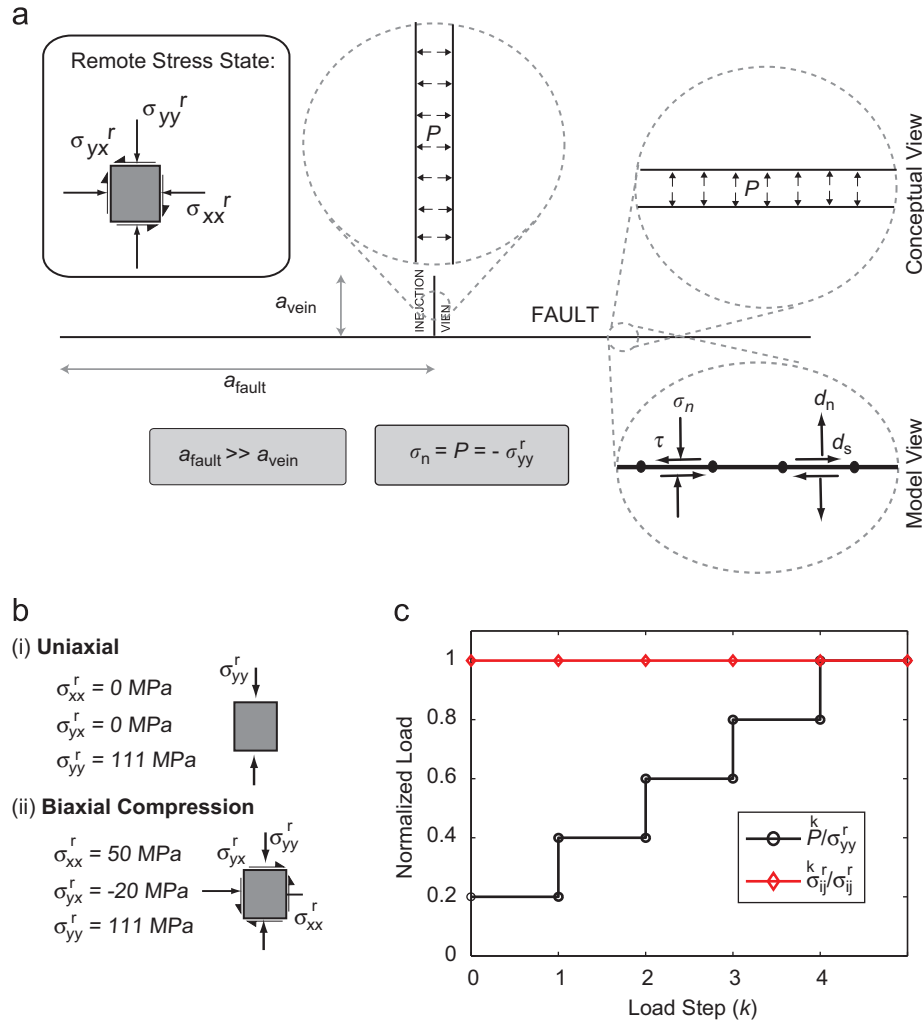

Fig. 5. Geometry, conceptual model for internal pressure on fault and injection vein, numerical representation of fault and injection vein, and boundary conditions for initial modeling of injection vein opening. Arrows in (a) representing remote stresses σ_{xx}^r, σ_{yy}^r, σ_{xy}^r, tractions τ_n, τ, and displacements d_n, d_s on faults are drawn as positive, whereas arrows in (b) indicate the remote stresses used in each case. Sign convention mimics that of Mutlu and Pollard (2008). Consistent with sign conventions used by Mutlu and Pollard (2008) compressive far-field (remote) normal stresses, compressive normal tractions acting on fault planes, and opening displacement discontinuities are all considered positive. Left-lateral shear tractions and right-lateral displacement discontinuities are positive. For example, in the global coordinate system, a far-field compressive remote stress σ_{yy}^r will be positive. Based on the sign convention used for stress in the fault element-local coordinate system ("Model View"), the sign of the melt fluid pressure P ("Conceptual View") is the opposite of the far field compressive stress, hence $P = \sigma_{yy}^r$.
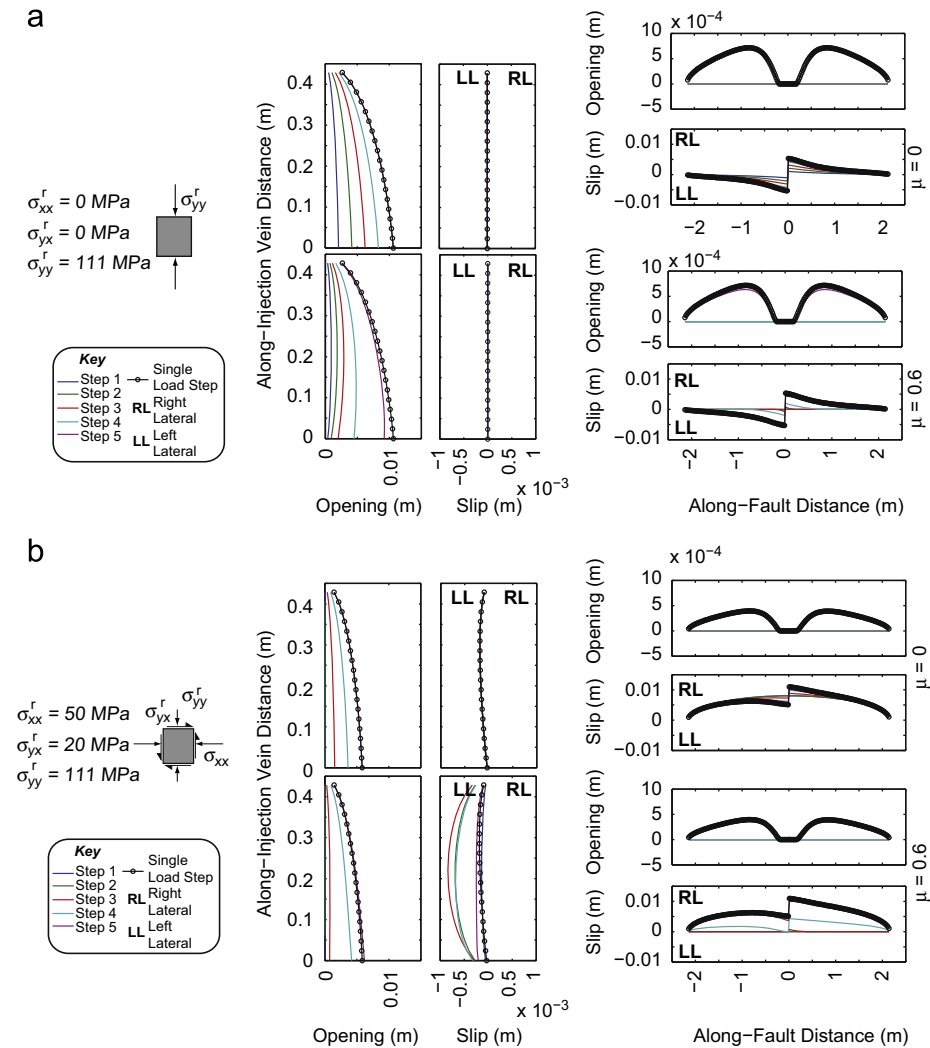
Fig. 6. Displacement distributions for an injection vein of measured length $a_{vein}=0.4285$ m and $E=20$ GPa for (a) Uniaxial and (b) Biaxial Compression remote stress boundary conditions. Note that aperture measured in the field for this injection vein is 0.0061 m. For each plot, modeled displacement distributions are shown as the cumulative slip at each load step (colored lines, Step 1–5) compared to a model in which fluid pressure P is applied in one single load step (black lines with circles at data points). For each loading case (*Uniaxial* or *Biaxial Compression*) both opening and sliding displacement profiles are shown for the injection vein (left) and fault vein (right) for friction coefficient $\mu=0.0$ (top) and $\mu=0.6$ bottom. For sliding displacements, right-lateral (RL) slips are positive while left lateral (LL) slip is negative. (For interpretation of references to color in this figure legend, the reader is referred to the web version of this article.)

in order to isolate fault-tip effects from the vein opening process. The fault and injection veins are assumed to be filled with melt with uniform pressure P. Consistent with recent constitutive models describing melt lubrication during fast slip (e.g. Nielsen et al., 2008, 2010), we assume that the magnitude of the fluid pressure is exactly the same as the fault-normal stress (σ_{yy}^r). In most instances, pseudotachylyte fault veins maintain a thin finite thickness varying locally but decorating the entire fault surface and keeping asperities from coming into contact (e.g. Hirose and Shimamoto, 2003; Di Toro et al., 2005a, 2006; Griffith et al., 2008, 2010). In order to maintain a thin layer of melt of roughly constant thickness on the fault throughout slip, P and σ_{yy}^r must reach an equilibrium (i.e. melt extrusion exactly balances melt production). This assumption has been shown to be valid for experimentally produced pseudotachylytes (Nielsen et al., 2008) and has been extended to the case of natural faults (Nielsen et al., 2010). In each simulation, the remote stress tensor, σ_{ij}^r, is held constant, and P is increased linearly through a series of five load steps from zero until it reaches the magnitude of σ_{yy}^r (Fig. 5c). We consider vein opening under a variety of remote biaxial stress states, and the DDM accounts for mechanical interaction between the injection and fault vein.

In each numerical model we prescribe injection vein length based on field measurements, and we calculate an array of apertures for each vein using systematically varying independent variables (model boundary conditions) and material constants. The model with the combination of independent variables and material constants producing the closest match (least misfit) to the maximum aperture measured in the field (the dependent variable) is deemed to be the physically most realistic model. Constants common to each simulation include the tractions prescribed on the model surfaces, the model geometry, and Poisson's ratio v, while the independent variables and material constants explored are Young's Modulus E, static friction coefficient μ, and the remote stress tensor σ_{ij}^r. Our goal is to isolate the effect of Young's Modulus E. Poisson's ratio in most cases is chosen to be $v=0.25$. We model static friction coefficients $\mu=0.0$ and 0.6, representing lower and upper limits on average sliding friction values for rock during rupture.

Two remote stress tensors representing a range of likely *in situ* conditions are examined based on the following considerations. Given an Andersonian strike-slip faulting regime for a critically stressed fault, coefficient of friction $\mu=0.75$, gravity $g=10$ m s^{-2}, and average density $\rho=2650$ kg m^{-3}, and pore fluid factor $\lambda=0.4$, horizontal principal stresses are$=254$ MPa and $\sigma_h^r=64$ MPa at

10 km depth, the estimated depth of the GLFZ (e.g., Di Toro et al., 2005b; Griffith et al., 2010). These conditions result in a fault-perpendicular stress, $\sigma_{yy}^r = 111$ MPa, a reasonable guess for the studied faults just *before* slip.

The remote stress tensors, intended to approximate the stress state after commencement of slip, are addressed as *Uniaxial* and *Biaxial Compression* in the following (Fig. 5b). These end member stress tensors share that (1) the fault-parallel normal stress component σ_{xx}^r (the normal stress acting perpendicular to the injection vein walls) is small compared to σ_{yy}^r, and (2) σ_{xy}^r is small compared to that of a critically stressed fault, both reasonable assumptions given that the process of injection vein opening happens soon after the local passage of a shear-rupture tip (e.g. Di Toro et al., 2005b). In addition, for all cases the fault-normal compressive stress is kept at $\sigma_{yy}^r = 111$ MPa as in the critically-stressed state in order to keep the peak melt pressure P the same for all simulations. For the *Uniaxial* case, we assume that σ_{xy}^r has been completely relieved (equal to zero), equivalent to assuming that the fault vein is completely lubricated and the shear stress is zero for a distance from the fault much greater than the length of the injection vein, and the fault-parallel compressive normal stress $\sigma_{xx}^r = 0$. In the *Biaxial Compression* case, $\sigma_{xx}^r = 50$ MPa, and $\sigma_{xy}^r = -20$ MPa, i.e., fault parallel stress and shear stress are relieved only partially. The partial relief is expected to more closely approximate the average transient stress state on the tensile side of the fault immediately after passage of a shear rupture.

We make no attempt to explicitly model the dynamically evolving stress state during and after earthquake rupture. Instead we choose two end members bracketing likely average stress states during vein opening. Reches and Dewers (2005) showed that the tensile stress perturbation near a propagating rupture tip can reach values of 5 GPa, yet this value is based on Linear Elastic Fracture Mechanics, and likely to be modulated by inelastic deformation (tensile failure). Furthermore, at significant depths, this tensile perturbation is likely to be limited in extent temporally and spatially. Di Toro et al. (2005b) showed using the solution for a propagating slip pulse (Rice et al., 2005) at the *in situ* stress conditions considered in the current study, that the fault-parallel length of the tensile domain associated with a propagating rupture tip is limited to 40–200 m considering a wide range of likely rupture velocities and stress drops. At a rupture velocity consistent with the Rayleigh wave speed for tonalite ($v_r \approx 2800$ m/s), the duration of this tensile perturbation should be limited to much less than 10^{-1} s. Given a range of quench times of 10^{-1} to 10^3 s (Rowe et al., in press), tensile stresses are unlikely to have persisted for the vast majority of injection veins. Therefore we prefer the interpretation that some recovery of the compressive fault-parallel normal stress (σ_{xx}^r) occurs during vein opening and cooling, and that the actual state of stress likely varied between the *Uniaxal* and *Biaxial Compression* cases.

Two friction coefficients ($\mu = 0$ and 0.6) are considered in simulations for each of a range of Young's modulus values, including possible values of 0.01, 0.05, 0.1, and 0.5 GPa as well as integers ranging from 1 to 80 GPa, resulting in 85 possible values for the Young's modulus for each injection vein. After each simulation, the opening displacement at the injection vein base is compared to the field measurement of vein aperture. The Young's modulus that produces the least misfit to aperture measured in the field is chosen as the best-fit effective Young's modulus (E_e) for the given boundary conditions. This procedure required roughly 30,000 individual simulations, each with five load steps.

4.3. Model results

Slip and opening distributions along the injection vein and fault vein calculated for an injection vein of measured length 0.4285 m, measured aperture 0.0061 m, and $E = 20$ GPa for the Uniaxial case (Fig. 6a) yield a larger peak opening displacement than the field measurement, therefore the best-fit Young's modulus must be greater than 20 GPa for this scenario. Comparing opening distributions for the uniaxial case with $\mu = 0.0$ and $\mu = 0.6$, we find that the addition of a non-zero friction coefficient causes frictional drag along the fault vein, resulting in "pinching" of the injection vein at the vein base in all five load steps (colored lines). For $\mu = 0.6$ the path-dependence is notable from the difference in final opening distribution for a single load step, resembling the one for $\mu = 0$, and for load-stepping, yielding slightly smaller opening with a maximum offset from the vein base. Slip does not occur along the injection vein as expected for uniaxial loading, however slip occurs along the fault vein for both friction coefficients. The sense of slip is consistent with accommodation of strain related to vein opening. Finally, fault vein opening only occurs during the final load step because $P < \sigma_{yy}^r$ until the final load step. In all simulations, the fault vein remains closed near the vein base, indicating that frictional contact of the fault walls exerts some control on injection vein opening. *Biaxial Compression* (Fig. 6b) results in vein opening displacements qualitatively similar to *Uniaxial* loading, except, as expected, maximum opening magnitude is smaller because pressure P is opposed by a non-zero far-field σ_{xx}^r. Sliding displacement across the injection vein occurs for both friction coefficients, consistent with the sense of the far-field shear stress, σ_{xy}^r. Slip along the fault vein is right-lateral for both friction coefficients as expected for the given sign of σ_{xy}^r.

The bulk of values of average best-fit effective Young's modulus E_e cluster between 1 and 11 GPa, with estimates for cataclasite generally lower than tonalite for each set of simulation conditions (loading case and friction coefficient) (Fig. 7, Table 1). Average E_e values considering all simulations were 0.8–4.2 GPa for cataclasite and 2.1–11.3 GPa for tonalite (Table 1). As expected, the *Uniaxial* case yields the largest average E_e, and the *Biaxial* Compression case yields the smallest average E_e. Friction coefficient only has a significant impact on E_e for the *Uniaxial* case, likely because slip on the fault vein is driven solely by opening of the injection vein, whereas in the *Biaxial Compression* case fault slip is driven by the non-zero far-field shear stress.

Effective moduli E_e exhibit a systematic length-dependence (Fig. 7). Apparent stiffness of the rocks increases as injection vein length increases. The largest estimated E_e value is associated with the longest measured injection vein ($a_{vein} = 428.5$ mm). For the *Uniaxial* case with $\mu = 0$, E_e in tonalite is 43 GPa, respectively, for this vein at the lower end of expected values for an intact tonalite (e.g., Birch, 1966). For *Biaxial Compression*, the corresponding result is only 10 GPa. The next-largest E_e calculated for each simulation is roughly 35% lower, and most of the data cluster below 10 GPa in the *Uniaxial* case and well below 5 GPa for the *Biaxial Compression* case (Fig. 7). This large range of E_e is also displayed by the large standard deviation of tonalite calculations (Table 1). Interestingly, standard deviation for cataclasites is substantially lower than for tonalite, perhaps owing to the fact that the length range of injection veins in cataclasites is much more narrow than the length range of veins in tonalite, the maximum injection vein length in cataclasites being $a_{vein} = 80$ mm.

We explored the effect of variations in Poisson's ratio ($0.1 \le \nu \le 0.5$) in simulations of an injection vein with 80 mm length and 4 mm aperture in order to assess the effect of assuming a constant value ($\nu = 0.5$) in our best-fit Young's modulus simulations. The results of this exploration show that regardless of choice of ν the best fit E_e varies only $+/-1$ GPa. This result does not imply that a significant coseismic decrease in E will not be accompanied by an increase in ν but simply confirms that our model is insensitive to changes in ν.
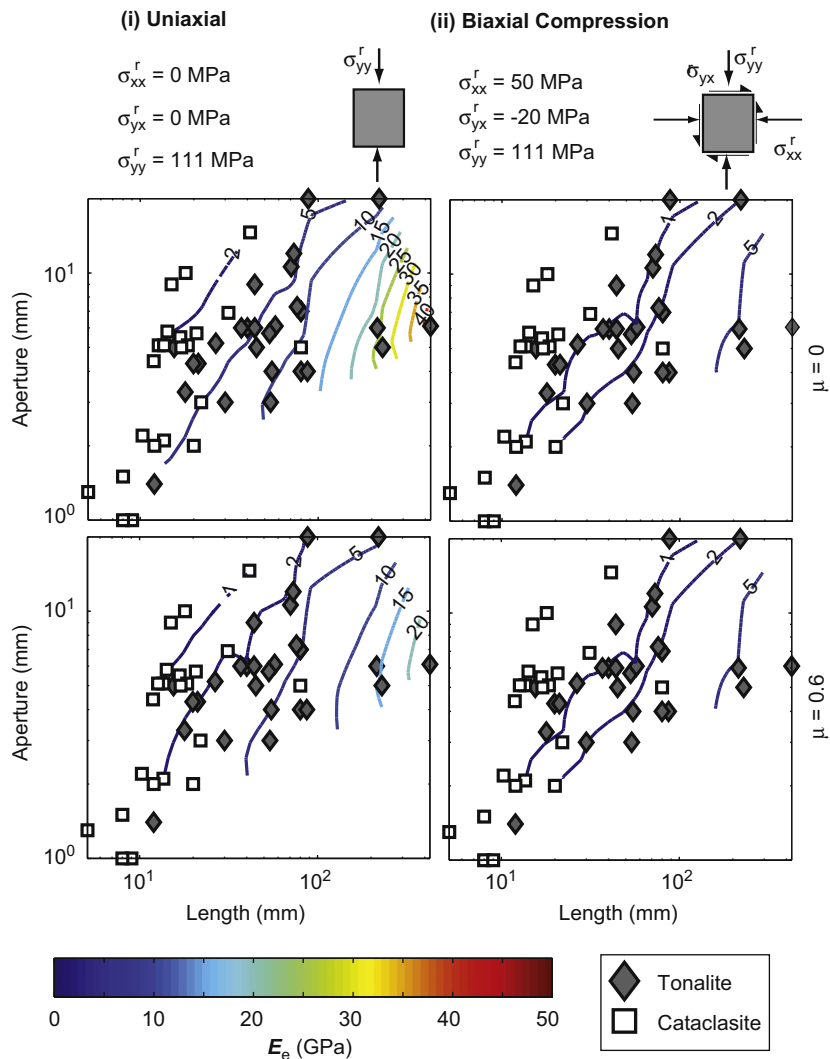
Fig. 7. Field measurements of aspect ratio vs. length contoured by best-fit Young's Modulus (E_e) in units of GPa. Like the displacement plots in Fig. 6, each column corresponds to results from each loading case (*Uniaxial*, *Biaxial*), and each row corresponds to a friction coefficient ($\mu = 0.0$ and 0.6). Colored contours are of E_e at units of 1, 2, 5, 10, 15, 20, 25, 30, 35, 40, 45, and 50 GPa (see colorbar). Note that the waviness of the contours is due to the discrete nature of the grid search in our approach: Possible Young's modulus values are largely restricted to being integers.

Table 1
General results from each set of simulations, arranged by loading case (Fig. 6) and friction coefficient.

Loading case	μ Dimensionless	Tonalite E_e				Cataclasite E_e			
		Mean (GPa)	Std (GPa)	Max (GPa)	Min (GPa)	Mean (GPa)	Std (GPa)	Max (GPa)	Min (GPa)
Uniaxial	0	8.4	8.9	43	2	3.2	2.1	10	1
"	0.6	4.9	5.2	25	1	1.9	1.3	6	0.5
Biaxial Comp	0	2.1	2.1	10	0.5	0.8	0.5	2	0.5
"	0.6	2.1	2.1	10	0.5	0.8	0.5	2	0.5
Uniaxial, n=1	0	7.6	7.1	33	2	3.1	1.9	9	1
Uniaxial, n=2	0	6.5	5.6	26	2	3.0	1.7	8	1
Uniaxial, n=3	0	5.6	4.7	22	2	2.7	1.5	7	1
Uniaxial, n=4	0	5.1	4.1	19	2	2.4	1.4	6	1

5. Laboratory rock mechanics tests

We directly measured elastic properties of rock samples taken from the GLFZ to compare the indirect constraints on coseismic stiffness gained from the modeling to constraints on post-exhumation elastic properties. Six samples, three of cataclasite and three of intact tonalite, were cored from blocks from the GLFZ

(Fig. 9a). We conducted constant-rate uniaxial loading experiments using a servo-hydraulically controlled rig with 500 t loading capacity on 30×75 mm oven dried cylindrical cores ground to strict tolerances (± 0.01 mm) as to the squareness of their edges. Steel spacers of 30 mm diameter were placed at either end of the sample to minimize end effects (Hawkes and Mellor, 1970). Principal strains were measured with commercial strain gauges
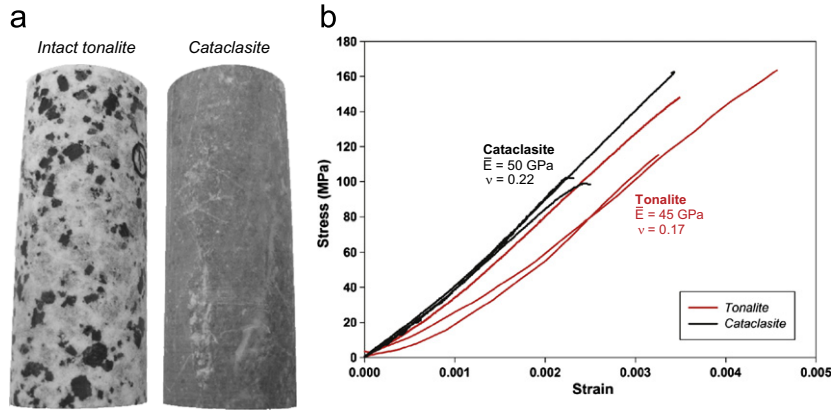
Fig. 8. Laboratory rock mechanics tests. (a) Cored samples of intact tonalite (left) and cataclasite (right). Samples are 75 mm long and 35 mm in diameter. (b) Comparison of axial strain vs. stress for both rocks, and related elastic moduli and Poisson ratios.

Table 2
Experimental results for uniaxial compressive strength (UCS), elastic modulus (E), and Poisson's ratio (v) of 6 intact samples.

Test no.	Rock type	UCS (MPa)	E (GPa)	v
T1	Tonalite	117	47	0.16
T2	Tonalite	164	42	0.18
T3	Tonalite	146	47	0.17
	Average	**142 ± 24**	**45 ± 3**	**0.17 ± 0.01**
C1	Cataclasite	103	53	0.33
C2	Cataclasite	161	51	0.17
C3	Cataclasite	98	45	0.16
	Average	**121 ± 35**	**50 ± 4**	**0.22 ± 0.10**

glued onto the samples in an axial and circumferential arrangement (Fig. 8b) and wired into full Wheatstone bridge circuits utilizing a dummy sample to minimize varying environmental effects. Axial load was measured with a load cell (accuracy 0.01%) and axial displacement with a coupled pair of displacement transducers (accuracy 0.2%). The axial piston was advanced at a constant velocity of 0.1 mm/min corresponding to a nominal axial strain rate of $\sim 2 \times 10^{-5}\,\text{s}^{-1}$ until sample failure. The actual strain rate of the sample is smaller by up to a factor of two due to system shortening.

For each experiment, axial (ε_{ax}) and circumferential strains (ε_{cir}) were measured as a function of applied stress (applied load divided by cross-sectional sample area), and volumetric strain (ε_v) was calculated assuming isotropic elastic behavior of the sample (i.e., $\varepsilon_v = \varepsilon_{ax} + 2\varepsilon_{cir}$). Young's modulus E and Poisson's ratio v were determined from the linear portion of the stress–strain curves (Fig. 8c and d, Table 2). The tested rocks may deviate from truly isotropic behavior, and the determined elastic parameters should ideally be referred to as apparent. The elastic moduli have relative accuracies of $\sim 10\%$, independent of intrinsic non-linear behavior. Cataclasite and tonalite have average Young's moduli of 50 GPa and 45 GPa, respectively, indicating that the cataclasite is the stiffer medium. Average ultimate compressive strengths and Poisson's ratio amount to 121 MPa and 143 MPa and 0.22 and 0.17 for cataclasite and tonalite, respectively.

6. Discussion

In the following discussion we successively address the effects of assumptions made in our simulations, potential sources of the

apparent length-dependence of E_e, and implications of our study results on fault zone healing.

6.1. Effects of model assumptions

Several assumptions were made in the numerical model, all of which have some effect on the results. While additional complexity could make the model more accurate, we focused on finding the most *conservative* estimate of coseismic stiffness reduction. For example, we model the process of injection vein opening as a 2D plane strain phenomenon. A more accurate model would represent injection veins as half-ellipsoidal cracks, as they do not extend indefinitely in and out of the plane of observation. However, the third dimension is difficult to constrain based on field observations. In any case, the maximum displacement across 3D ellipsoidal cracks will generally be smaller than displacements along 2D plane strain cracks for equal rock properties and driving stress, because the 3D crack tip line provides more resistance to opening than an infinitely long crack. Thus for a given opening, the E_e value calculated using a 3D crack model will be smaller than that calculated for a 2D model. Consequently, Young's moduli calculated in our simulations reflect the *largest possible* value of Young's modulus during and shortly after the earthquake associated with the observed injection veins. In reality the stiffness reductions are likely to have been greater.

6.2. Dependence of E_e on a_{vein}

The numerical estimate of Young's modulus correlates with the injection vein length (Fig. 7). Specifically, for tonalite, the longer the vein as measured in the field, the larger (and closer to the expected intact value) is E_e. Injection vein opening is driven by fluid overpressure ($P - \sigma_{xx}^r$) and opposed by elastic stiffness, therefore spatial gradients in either (or both) of these factors can be responsible for the length-dependence of the calculated effective Young's moduli. For example, a gradient in the fluid overpressure may have a hydrodynamic cause, i.e., reduction of P_{vein} with distance from the fault, or may reflect a heterogeneous stress field in which the fault-parallel normal stress increases away from the fault. Likewise, a gradient in elastic stiffness might be the result of a decrease in damage density away from the fault reaching undamaged conditions at a distance perpendicular to the fault of less than 428.5 mm. Unfortunately, using the current model, these factors (damage, melt pressure, and stress gradients) are inseparable, but their effects likely simultaneously contribute to the apparent stiffening of rocks with distance from the fault indicated by the length-dependence. We can however explore
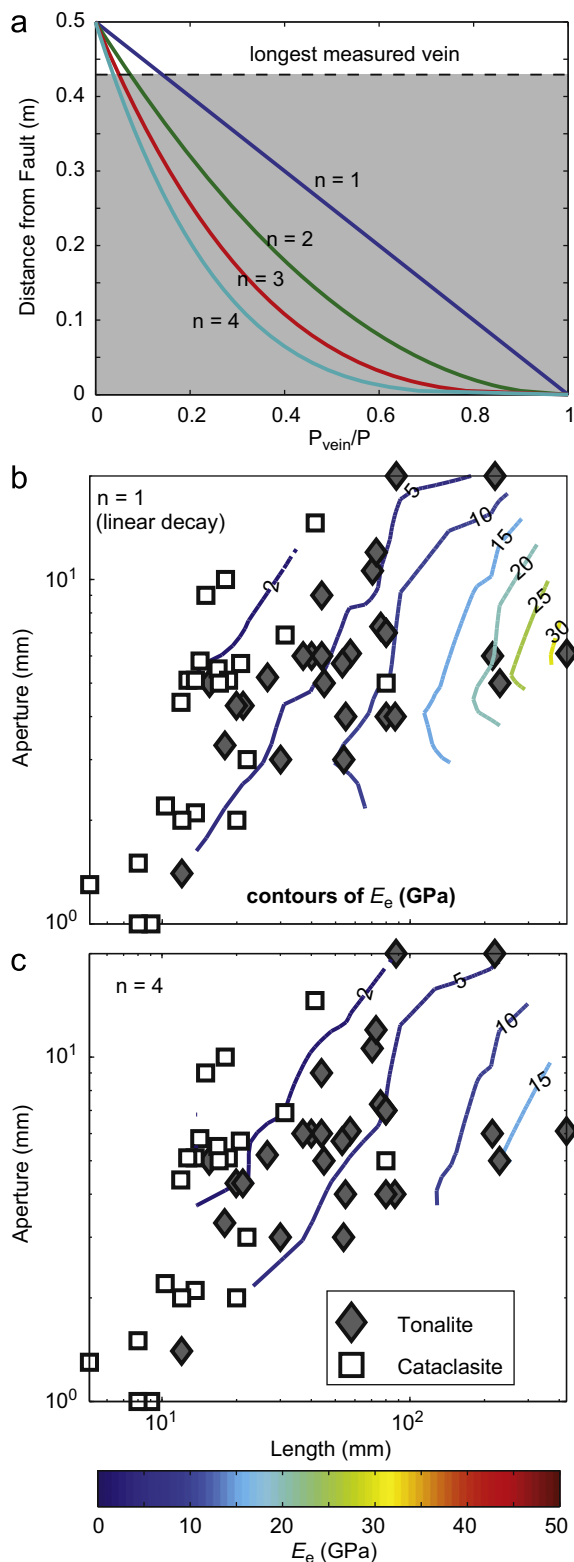
Fig. 9. E_e (in GPa) calculated using a pressure gradient in the injection vein (Eq. (1) in the text). (a) Solutions of Eq. (1): for $n=1$, the pressure decay is linear with distance from the fault; for $n=4$, the pressure decay is rapid near the fault. (b) In the case of a linear decay ($n=1$) of the melt pressure in the injection vein, the calculated E_e are in the range of 1–30 GPa. (c) In the case of a non-linear decay ($n=4$) of the melt pressure in the vein, the calculated E_e are in the range of 1–15 GPa. Nearly all calculated Young's Modulus values collapse into the range of 1–15 GPa as a result of the pressure gradient in the injection vein. The modeled pressure gradient captures potential effects of fluid pressure gradient, remote stress field gradients, and damage gradients, and it is likely that each plays a role.

their total effect on the calculated Young's moduli by prescribing a pressure gradient along the injection vein elements decaying from P at fault vein ($y=0$) to zero at a distance equivalent to the longest injection vein ($y \approx 0.5$ m):

$$P_{\text{vein}} = P\left[1-\left(\frac{y}{0.5}\right)^{1/n}\right], \, 0 \le y \le a_{\text{vein}} \qquad (1)$$

The exponent $1/n$ characterizes the pressure decay. For $n=1$, the pressure decays linearly from P at the injection vein tip to zero at $y=0.5$ m.

For brevity we discuss the effect of such a pressure gradient only for the *Uniaxial* case with $\mu=0$. A linear decay ($n=1$, Fig. 9b) results in reduction of E_e values compared to the previous calculations for constant fluid pressure in the vein, however the longest vein still yields an E_e value of 33 GPa (Table 1), close to intact values and still more than an order of magnitude larger than values for the shortest veins. With $n=4$, the range of E_e values collapses significantly, as indicated by the smaller standard deviation of 4.1 GPa (Table 1), with only the longest vein returning a value of $E_e=19$ GPa. The two quantities E and σ_{ij}^r are uniform in each model, and we thus model the net effect of variations in P, σ_{ij}^r, and damage (assumed to be the primary mechanism for stiffness reduction) by prescribing a variation in P_{vein}. For non-vanishing contributions of variations in the other two parameters, the actual fluid pressure gradient was likely less dramatic than the gradient given by Eq. (1) with $n=4$.

Because the E_e values collapse into a small range for $n=4$, a likely scenario is that the net effect of a gradient in fluid pressure, stress heterogeneity, and damage was restricted to a width of less than 0.5 m along each fault strand. This conclusion is corroborated by the observation that the opening distribution along injection veins is decidedly non-elliptical but more closely resembles a half-bell shape instead of a half-ellipse (Fig. 1). Such an opening distribution is qualitatively similar to cohesive endzone models of opening mode cracks, in which opening near the tip of the crack is opposed by cohesive tractions in a finite-length region near the crack tip (e.g., Dugdale, 1960; Barenblatt, 1962). The tractions acting within the cohesive endzone can mimic a variety of processes, including inelastic deformation (distributed microfracturing or high strain-rate plastic deformation) within the crack process zone, variations of elastic moduli, or actual changes in tractions acting on the crack face. In the current case, we contend that the observed non-elliptical opening distribution is likely a product of decreasing damage and melt pressure away from the fault, and possibly stress field heterogeneity.

Finally, the width of the zone of rock that interacts with a propagating earthquake rupture scales with the rupture dimension. Therefore a damage zone less than a meter thick by itself would have exerted little effect on the overall earthquake energy budget for moderate and large ruptures. However, if similar, or even partially healed, damage were to persist throughout the seismic history for the hundreds of individual fault strands across the roughly 500 m wide zone composing the GLFZ, the resulting modulus reduction could be significant for moderate to large earthquakes.

6.2. Implication for healing from comparison of E_e and E_{lab}

What is perhaps most provocative about our results is the magnitude of *in situ* Young's Modulus reduction compared to (a) generally expected values of crystalline rocks at depth and (b) measured values of samples from the investigated area. Average simulated values of coseismic Young's modulus (E_e) range from 2.1 to 8.4 GPa for tonalite and 1 to 3.2 GPa for cataclasite (Table 1), whereas laboratory measurements yield E_{lab} values of 42–47 GPa for tonalite and 45–53 GPa for cataclasite (Table 2).

These values imply a coseismic *in situ* reduction in E by a factor of 5–20 for tonalite relative to the current state, and a factor of 15–50 for cataclasite.

Some discrepancy between laboratory and outcrop values is expected. A scale effect of rock stiffness measurements due to the presence of structural discontinuities has been well documented in the engineering rock mechanics literature (Bieniawski, 1984); however the large difference between E_{lab} and E_e in the current study coupled with field observations that microcracks and cataclasites have been healed by precipitated minerals suggests that *in situ* stiffness values were transient and significant post-seismic healing occurred. Interestingly, the numerical model predicts that coseismically damaged tonalite is the relatively stiffer rock, whereas the laboratory results suggest that exhumed cataclasite is at least as stiff as exhumed tonalite. The cataclasite is a fault rock likely derived from intact tonalite progressively fractured, altered by fluid-rock interaction at subgreenschist facies conditions and comminuted during faulting (Di Toro and Pennacchioni, 2005). As such, the cataclasitic rock presumably had a reduced stiffness relative to that of the original protolith at the time of formation. Based on cross-cutting relationships, however, Di Toro and Pennacchioni (2005) interpreted cataclasite induration to predate or be (geologically) synchronous with pseudotachylyte generation, therefore healing occurred prior to exhumation, likely during the seismic cycle. Given that average E_e of cataclasite is significantly less than that of the tonalite, a likely conclusion is that interseismic healing progressed less than for the tonalite, and that longer-term healing at relatively constant pressure-temperature conditions (i.e., prior to exhumation) was required to bring the cataclasite stiffness to at least that of the tonalite. Comparable ultimate strengths for the cataclasite and tonalite (Table 2) indicate that the cataclasites have also regained significant strength following induration and healing.

7. Conclusions

Length to aperture ratios of pseudotachylyte injection veins where the injection veins intrude cataclastic fault rocks are systematically smaller than the same ratios where injection veins intrude tonalite in the Gole Larghe Fault Zone. Our simulations of pseudotachylyte injection vein opening aiming at reproducing the observed length to aperture ratios show that tonalites were stiffer than cataclasites during the final stage of vein development by an average factor of two to three, consistent with pseudotachylyte production prior to complete healing of cataclasites. Modeling indicates that vein opening magnitude is influenced by tractions induced on the main fault surface during deformation AND remote stress components in addition to fault parallel normal stress. Variations in Poisson's ratio have little effect in the present context. According to our simulations, the *in situ* coseismic stiffness of all fault rocks was small compared to general expectations for intact rocks and at least a factor of 5–50 smaller than laboratory measurements on the now exhumed rocks pointing to significant coseismic stiffness reduction. The disagreement between laboratory measurements and simulations brings into question the appropriateness of using laboratory-derived values for rock stiffness to model coseismic processes at depth. Analogously, parameters affected by damage, including Young's modulus, permeability, compressibility, and thermal expansivity, may vary significantly enough on short timescales close to the fault to largely disagree with laboratory-derived measurements on exhumed rock.

References

Barenblatt, G.I., 1962. The mathematical theory of equilibrium cracks in brittle fracture. Adv. Appl. Mech. 7, 55–80.

Biegel, R.L., Sammis, C.G., Rosakis, A.J., 2008. An experimental study of the effect of off-fault damage on the velocity of a slip pulse. J. Geophys. Res. 113, B04302 http://dx.doi.org/10.1029/2007JB005234.

Bieniawski, Z.T., 1984. Rock Mechanics Design in Mining and Tunneling. A.A. Balkema, Rotterdam (272 p).

Birch, F., 1966. Compressibility: elastic constants. In: Clark, P. (Ed.), Handbook of Physical Constants, Geological Society of America, New York, 587 pp.

Brantley, S.L., Evans, B., Hickman, S.H., Crerar, D.A., 1990. Healing of microcracks in quartz—implications for fluid-flow. Geology 18, 136–139.

Brenguier, F., Campillo, M., Hadziioannou, C., Shapiro, N.M., Nadeau, R.M., Larose, E., 2008. Postseismic relaxation along the San Andreas fault at Parkfield from continuous seismological observations. Science 321, 1478–1481.

Cochran, E., Li, Y.-G., Shearer, P., Barbot, S., Fialko, Y., Vidale, J., 2009. Seismic and geodetic evidence for extensive, long-lived fault damage zones. Geology 37, 315–318.

Crouch, S.L., Starfield, A.M., 1983. Boundary Element Methods in Solid Mechanics. George Allen & Unwin, London. (322 p).

De Bremaecker, J.C., Ferris, M.C., 2004. Numerical models of shear fracture propagation. Int. J. Fract. 21, 2161–2178.

Delaney, P.T., Pollard, D.D., 1981. Deformation of host rocks and flow of magma during growth of minette dikes and breccias-bearing intrusions near Ship Rock, New Mexico. Geological Society Professional Paper 1202.

Delaney, P.T., Pollard, D.D., Ziony, J.I., McKee, E.H., 1986. Field relations between dikes and joints: emplacement processes and paleostress analysis. J. Geophys. Res. 91 (B5), 4920–4938.

Di Toro, G., Pennacchioni, G., 2004. Superheated friction-induced melts in zoned pseudotachylytes within the Adamello tonalites (Italian Southern Alps). J. Struct. Geol. 26, 1783–1801.

Di Toro, G., Pennacchioni, G., 2005. Fault plane processes and mesoscopic structure of a strong-type seismogenic fault in tonalites (Adamello batholith, Southern Italian Alps). Tectonophysics 402, 55–80.

Di Toro, G., Pennacchioni, G., Teza, G., 2005a. Can pseudotachylytes be used to infer earthquake source parameters? An example of limitations in the study of exhumed faults. Tectonophysics 402, 3–20.

Di Toro, G., Nielsen, S., Pennacchioni, G., 2005b. Earthquake dynamics frozen in exhumed ancient faults. Nature 436, 1009–1012.

Di Toro, G., Hirose, T., Nielsen, S., Pennacchioni, G., Shimamoto, T., 2006. Natural and experimental evidence of melt lubrication of faults during earthquakes. Science 311, 647–649.

Dugdale, D.S.J., 1960. Yielding of steel sheets containing slits. Mech. Phys. Solids 8, 100–115.

Faulkner, D.R., Mitchell, T.M., Healy, D., Heap, M.J., 2006. Slip on "weak" faults by the rotation of regional stress in the fracture damage zone. Nature, 444, http://dx.doi.org/10.1038/nature05353.

Gratier, J.P., Favreau, P., Renard, F., 2003. Modeling fluid transfer along California faults when integrating pressure solution crack sealing and compaction processes. J. Geophys. Res., 108, http://dx.doi.org/10.1029/2001JB000380.

Griffith, W.A., DiToro, G., Pennacchioni, G., Pollard, D.D., 2008. Thin pseudotachy-lytes in faults of the Mt. Abbot Quadrangle, Sierra Nevada: Physical constraints for seismic slip. J. Struct. Geol. 30, 1186–1194.

Griffith, W.A., Rosakis, A., Pollard, D., Ko, C.-W., 2009. Dynamic rupture experiments elucidate tensile crack development during propagating earthquake ruptures. Geology 37, 795–798.

Griffith, W.A., Nielsen, S., Di Toro, G., Smith, S.A.F., 2010. Rough faults, distributed weakening, and off-fault deformation. J. Geophys. Res. 115, B08409, http://dx.doi.org/10.1029/2009JB006925.

Grocott, J.R., 1981. Fracture geometry of pseudotachylyte generation zones: a study of shear fractures formed during seismic events. J. Struct. Geol. 3, 169–178.

Hawkes, I., Mellor, M., 1970. Uniaxial testing in rock mechanics laboratories. Eng. Geol. 4, 177–285.

Hiramatsu, Y., Honma, H., Saiga, A., Furumoto, M., Ooida, T., 2005. Seismological evidence on characteristic time of crack healing in the shallow crust. Geophys. Res. Lett. 32, 1–4.

Hirose, T., Shimamoto, T., 2003. Fractal dimension of molten surfaces as a possible parameter to infer the slip-weakening distance of faults from natural pseudotachylytes. J. Struct. Geol. 25 (10), 1569–1574.

Lachenbruch, A.H., 1980. Frictional heating, fluid pressure, and the resistance to fault motion. J. Geophys. Res. 85, 6097–6112.

Li, Y.-G., Aki, K., Adams, D., Hasemi, A., Lee, W.H.K., 1994. Seismic guided waves trapped in the fault zone of the Landers, California, earthquake of 1992. J. Geophys. Res. 99, 11705–11722.

Li, Y.-G., Vidale, J.E., Aki, K., Xu, F., Burdette, T., 1998. Evidence of shallow fault zone strengthening after the 1992 M7.5 Landers, California, Earthquake. Science 279, 217–219, http://dx.doi.org/10.1126/science.279.5348.217.

Li, Y.G., Chen, P., Cochran, E.S., Vidale, J.E., Burdette, T., 2006. Seismic evidence for rock damage and healing on the San Andreas Fault associated with the 2004 M 6.0 Parkfield Earthquake. Bull. Seismol. Soc. Am. 96 (4B), S349–S363, http://dx.doi.org/10.1785/0120050803.

Maddock, R.H., Grocott, J., VanNes, M., 1987. Vesicles, amygdales and similar structures in fault-generated pseudotachylytes. Lithos 20, 419–432.

Moore, D.E., Lockner, D.A., Byerlee, J.D., 1994. Reduction of permeability in granite at elevated temperatures. Science 265, 1558–1561.

Morrow, C.A., Moore, D.E., Lockner, D.A., 2001. Permeability reduction in granite under hydrothermal conditions. J. Geophys. Res. 106 (B12), 30551–30560.

Mutlu, O., Pollard, D.D., 2008. On the patterns of wing cracks along an outcrop scale flaw: a numerical modeling approach using complementarity. J. Geophys. Res. 113, B06403, http://dx.doi.org/10.1029/2007JB005284.

Ngo, D., Huang, Y., Rosakis, A., Griffith, W.A., Pollard, D.D., 2012. Off-fault tensile cracks: a link between geological fault observations, lab experiments, and dynamic rupture models. J. Geophys. Res., 117, http://dx.doi.org/10.1029/2011JB008577.

Nielsen, S., Di Toro, G., Hirose, T., Shimamoto, T., 2008. Frictional melt and seismic slip. J. Geophys. Res. 113, B01308.

Nielsen, S., Di Toro, G., Griffith, W.A., 2010. Friction and roughness of a melting rock surface. Geophys. J. Int. 182, 299–310.

Noda, H., Shimamoto, T., 2005. Thermal pressurization and slip-weakening distance of a fault: an example of the Hanaore Fault, southwest Japan. Bull. Seismol. Soc. Am. 95 (4), 1224–1233.

Pennacchioni, G., Di Toro, G., Brack, P., Menegon, L., Villa, I.M., 2006. Brittle-ductile-brittle deformation during cooling of tonalite (Adamello, Southern Italian Alps). Tectonophysics 427, 171–197.

Pollard, D.D., Holzhausen, G., 1979. On the mechanical interaction between a fluid-filled fracture and the earth's surface. Tectonophysics 53, 27–57.

Reches, Z., Dewers, T.A., 2005. Gouge formation by dynamic pulverization during earthquake rupture. Earth Planet. Sci. Lett. 235, 371–374.

Rice, J.R., 1992. In: Evans, B., Wong, T.-f. (Eds.), Fault Mechanics and Transport Properties of Rocks, Academic Press, San Diego, CA, pp. 475–503.

Rice, J.R., Sammis, C.G., Parsons, R., 2005. Off-fault secondary failure induced by a dynamic slip-pulse. Bull. Seismol. Soc. Am. 95 (1), 109–134.

Rice, J.R., 2006. Heating and weakening of faults during earthquake slip. J. Geophys. Res., 111, http://dx.doi.org/10.1029/2005JB004006.

Rowe, C.D., Kirkpatrick, J.D., Brodsky, E.E., 2012. Fault rock injections record paleo-earthquakes. Earth Planet. Sci. Lett. 335–336, 154–166.

Rubin, A.M., 1995. Propagation of magma-filled cracks. Annu. Rev. Earth Planet. Sci. 23, 287–336.

Sanford, R.J., 2003. Principles of Fracture Mechanics. Pearson Education, Inc., Upper Saddle River, NJ (404p).

Sibson, R.H., 1975. Generation of pseudotachylyte by ancient seismic faulting. Geophys. J. R. Astron. Soc. 43, 775–794.

Swanson, M.T., 1992. Fault structure, wear mechanisms and rupture processes in pseudotachylyte generaton. Tectonophysics 204, 223–242.

Tenthorey, E., Cox, S.F., 2006. Cohesive strengthening of fault zones during the interseismic period: an experimental study. J. Geophys. Res., 111, http://dx.doi.org/10.1029/2005JB004122.

Tenthorey, E., Fitz Gerald, J.D., 2006. Feedbacks between deformation, hydrothermal reaction and permeability evolution in the crust: experimental insights. Earth Planet. Sci. Lett. 247, 117–129.

Vidale, J.E., Li, Y.G., 2003. Damage to the shallow Landers fault from the nearby Hector Mine earthquake. Nature 421 (6922), 524–526.

Zoback, M., S., Hickman, W., Ellsworth, 2010. Scientific drilling into the San Andreas Fault Zone. Eos Trans, AGU, 91, 22. Doi: 10.1029/2010EO220001.